Nanoscale

ROYAL SOCIETY OF CHEMISTRY

PAPER

View Article Online
View Journal | View Issue

Cite this: *Nanoscale*, 2025, **17**, 13378

CVD synthesis and optical study of bandgap-tunable Sn-doped monolayer molybdenum disulfide†

Yuxin Zhang,[a,b] Zhengbo Zhong,[b] Yuhao Mi,[b] Jiawei Duan,[b] Sheng Han, *[a] Tianhui Ren *[b] and Zhipeng Li *[b]

Received 16th December 2024,
Accepted 28th April 2025

DOI: 10.1039/d4nr05288a

rsc.li/nanoscale

Two-dimensional transition metal dichalcogenides (TMDCs) have attracted extensive interest in next-generation optoelectronic devices and energy-harvesting absorbers due to their fascinating optical and electronic properties. It is of great interest to engineer the electronic structure of TMDCs to attain more intriguing physical properties. Here, we introduce $SnCl_2$ as a low-cost, environmentally friendly dopant to simultaneously engineer the band structure of monolayer MoS_2 and this is an easily scalable and high-quality, efficient one-step CVD method, revealing that the tensile strain induced by the different bond lengths of Sn–S and Mo–S can directionally modulate the electronic state of monolayer MoS_2 and lead to bandgap reforming, providing a feasible way for bandgap engineering. Our work demonstrates the effective modulation of TMDC's bandgap to expand the novel optoelectronic properties of 2D materials.

Introduction

Two-dimensional transition metal dichalcogenides have promising potential for diverse applications in optoelectronic devices,[1] quantum information science,[2] biomedicine,[3] and integrated circuits[4,5] because of their thickness-dependent bandgaps and unique electronic and optical properties. Among them, single-layer TMDCs as direct bandgap semiconductors,[6] such as monolayer molybdenum disulfide (MoS_2), are pertinent candidates for next-generation optoelectronic and valleytronic devices.[7] Currently, both top-down and bottom-up preparation techniques are developed to produce monolayer TMDCs, including mechanical cleavage,[7] liquid phase exfoliation,[8] physical vapor deposition (PVD),[9,10] molecular beam epitaxy (MBE)[11] and chemical vapor deposition (CVD).[12,13] Nevertheless, CVD is considered to be the most effective approach for large-scale and high-quality growth of 2D TMDCs.[14,15]

Two-dimensional semiconductors have tunable intermediate physical properties between insulators and conductors.[16] Chemical doping, a process that introduces charge carriers into semiconductors, is considered to be an effective way to control the optical and electronic performances of 2D materials.[17,18] In the case of surface chemical doping, the dopant is usually introduced into the 2D semiconductor through physical or chemical interactions without destroying the structure.[19,20] This is usually achieved by chemical treatments or solvent-based intercalation methods, and the choice of dopant can be generic, including small molecules, ions, and particles.[21,22] However, doped structures lack a covalent connection between the dopant and the TMDC, and may be in a metastable state that does not permanently maintain the endowed properties.[23] In contrast, substitutional doping, in which some of the sites in the original 2D lattice are exchanged by exogenous atoms, has been widely used in the engineering of band structures and phase transitions. Generally, it is achieved by employing a powder vaporization chemical vapor deposition (CVD) method and introducing all the reactant precursors together during the growth of crystals.[24] This integrated approach results in stable substitutional doped structures, but the challenge is to produce high-quality homogeneous single crystals due to the different crystallization temperatures of the target 2D materials and the evaporation rates of each precursor.

Many efforts have been made to find high-quality 2D single crystals, including the employment of sodium halides to passivate defects and enhance photoluminescence,[25] the salt-assisted CVD growth to modulate the defects of sulfur vacancies in MoS_2,[26] spontaneous n-doping caused by alkali metal compounds,[27] thermal oxidation-induced doping and etching in monolayer TMDs,[28] *in situ* gold chloride doping to

[a]*School of Chemical and Environmental Engineering, Shanghai Institute of Technology, Shanghai, 201418, China. E-mail: hansheng654321@sina.com*
[b]*School of Chemistry and Chemical Engineering, Shanghai Jiao Tong University, Shanghai, 200240, China. E-mail: li_zp1314@sjtu.edu.cn, thren@sjtu.edu.cn*
† Electronic supplementary information (ESI) available. See DOI: https://doi.org/10.1039/d4nr05288a

modulate the photo-responsive performance,[29] Nb doping to create a monolayer p–n diode,[30] vanadium doping to fabricate specific transistors[31] *etc*. It is worth noting that Sn has been proven to be an effective doping candidate.

Chang *et al.* used SnS as a precursor to post-substitute CVD-grown WS_2 to obtain a series of Sn/W/S composite 2D materials, which enables direct selective layer doping in bilayer crystals.[32] Olding *et al.* utilized pulsed MOCVD for low-temperature epitaxial growth of *ortho*-eutectic SnS on hexagonal MoS_2 and found the preference of layer-by-layer 3D growth with prolonging purge time between alternating precursor doses, thus providing good control over the film thickness.[33] Fu *et al.* used a NaCl-assisted space-confined CVD method to obtain a MoS_2/SnS_2 bilayer heterostructure and found the maximum responsivity of 9611 A W^{-1} under visible light irradiation and the minimum response time of ~510 μs.[34] However, most of the current progress has focused on combining Sn with 2D materials using a two-step method to modify the lattice structure to tune the photoluminescence characteristics and electrical properties. Therefore, is it possible to incorporate Sn and TMDC in a one-step CVD process to generate a Sn-doped TMDC with unique optical properties?

In this work, we innovatively introduce anhydrous stannous chloride ($SnCl_2$) as a dopant for monolayer MoS_2 growth *via* a simple and efficient one-step CVD method, and low-cost, environmentally friendly, easily scalable and high-quality Sn-doped MoS_2 monolayer single crystals are synthesized. The study of these systems will help us to establish a more comprehensive theoretical model of MoS_2 doping, develop doping materials with unique functionalities, and expand the applications of MoS_2 in emerging fields such as spintronics and quantum devices.

Results and discussion

Synthesis of Sn-doped monolayer MoS_2

Molybdenum disulfide (MoS_2) has a distinctive layer structure, high photoluminescence and low dark current; moreover, the bandgap can be restructured by layer thickness.[35] Pristine MoS_2 and 6 wt% $SnCl_2$-doped monolayer MoS_2 (Sn-doped MoS_2) were synthesized using a 2-inch tube furnace as shown in Fig. 1(a and b). The detailed synthesis procedure can be referred to the Methods section. Fig. 1(c) and (d) show the optical images of pristine and Sn-doped monolayer MoS_2 single crystals, both of which exhibit apparently triangular shapes, reflecting the 3-fold rotation symmetry and the high-quality single crystal nature. We first characterized the PL spectra of pristine MoS_2 and Sn-doped MoS_2 at room temperature and low temperature (77 K) as shown in Fig. 1(e) and (f), respectively, in which the pristine and Sn-doped MoS_2 manifest distinct emission features. At room temperature (~300 K, Fig. 1(e)), the A exciton of Sn-doped MoS_2 experiences a significant blueshift with an energy difference of ~60 meV from 1.783 eV to 1.856 eV, while the B exciton undergoes a relatively slight blueshift with an energy difference of ~10 meV from 1.889 eV to 1.901 eV compared with pristine MoS_2. At 77 K, the linewidth of exciton peaks becomes narrow and each exciton peak can be separately resolved (Fig. 1(f)), in which both the A and B excitons of Sn-MoS_2 show a 60 meV blueshift compared to pristine MoS_2. In addition, the peak located at ~1.728 eV is attributed to the localized defect-related exciton feature, which also presents a 20 meV blueshift. The results obviously indicate that the introduced $SnCl_2$ plays a vital role in the band structure renormalization of monolayer MoS_2. Therefore, we performed a systematic study of the influence of temperature and doping concentration on the CVD growth of Sn-doped MoS_2.

As shown in Fig. 1(g), 6 wt% $SnCl_2$ doped MoS_2 crystals were prepared at the temperatures of 650 °C, 700 °C, 750 °C and 800 °C, respectively. At 650 °C, Sn-doped MoS_2 crystals mainly show triangular shapes with obvious crystal boundaries and the lateral dimension of the nanosheet is ~10 μm. However, the low reaction temperature leads to relatively insufficient sulfur vapor for reaction with the MoO_3 vapor, which results in the incomplete growth of the crystal edges. When the temperature is increased to 700 °C, the deposited Sn-doped MoS_2 single crystals also show relatively uniform triangular shapes, but the nucleation density of the grown crystals is significantly reduced and the boundaries are smooth with an average lateral size up to ~13 μm. However, when the temperature is further increased to 750 °C, the nucleation density begins to increase and the growth starts to turn into the vertical direction with the increasing thickness of growth crystals. If the temperature is increased to 800 °C, the generated crystals show a cluster-like structure with prominent surface roughness, indicating too rigorous growth conditions for the MoS_2 single crystal. Therefore, we selected the growth temperature of 700 °C to explore the influence of $SnCl_2$ concentration on the properties of Sn-doped MoS_2.

Fig. 1(h) presents the optical images of pristine MoS_2 and 3 wt%, 6 wt% and 12 wt% Sn-doped MoS_2 (percentage of precursors) prepared at a temperature of 700 °C. Both the pristine MoS_2 and Sn-doped MoS_2 display relatively uniform triangular shapes. However, with the increasing $SnCl_2$ concentration, the morphologies of MoS_2 experience dramatic variations. Compared with the pristine MoS_2, the lateral dimensions of the crystals continuously shrink with the increase of $SnCl_2$ concentration, which might originate from the relatively huge difference of lattice constants between SnS (SnS_2) and MoS_2, limiting the growth of large areas of the single crystals. In addition, when the doping concentrations are 3 wt% and 12 wt%, most of the growth crystals undergo secondary growth accompanied by more Sn atoms adsorbed on the crystal surface, which might affect the overall growth efficiency and the physical properties of MoS_2. Nevertheless, the crystals grown from 6 wt% $SnCl_2$ doped MoS_2 exhibit homogeneous surface morphologies similar to pristine MoS_2 with an average crystal size of ~10 μm. It can be seen that the doping concentration of $SnCl_2$ greatly imposes the growth behaviors of MoS_2, thus might induce significant modulation of the crystal structure and optoelectronic properties, evidenced by the promi-

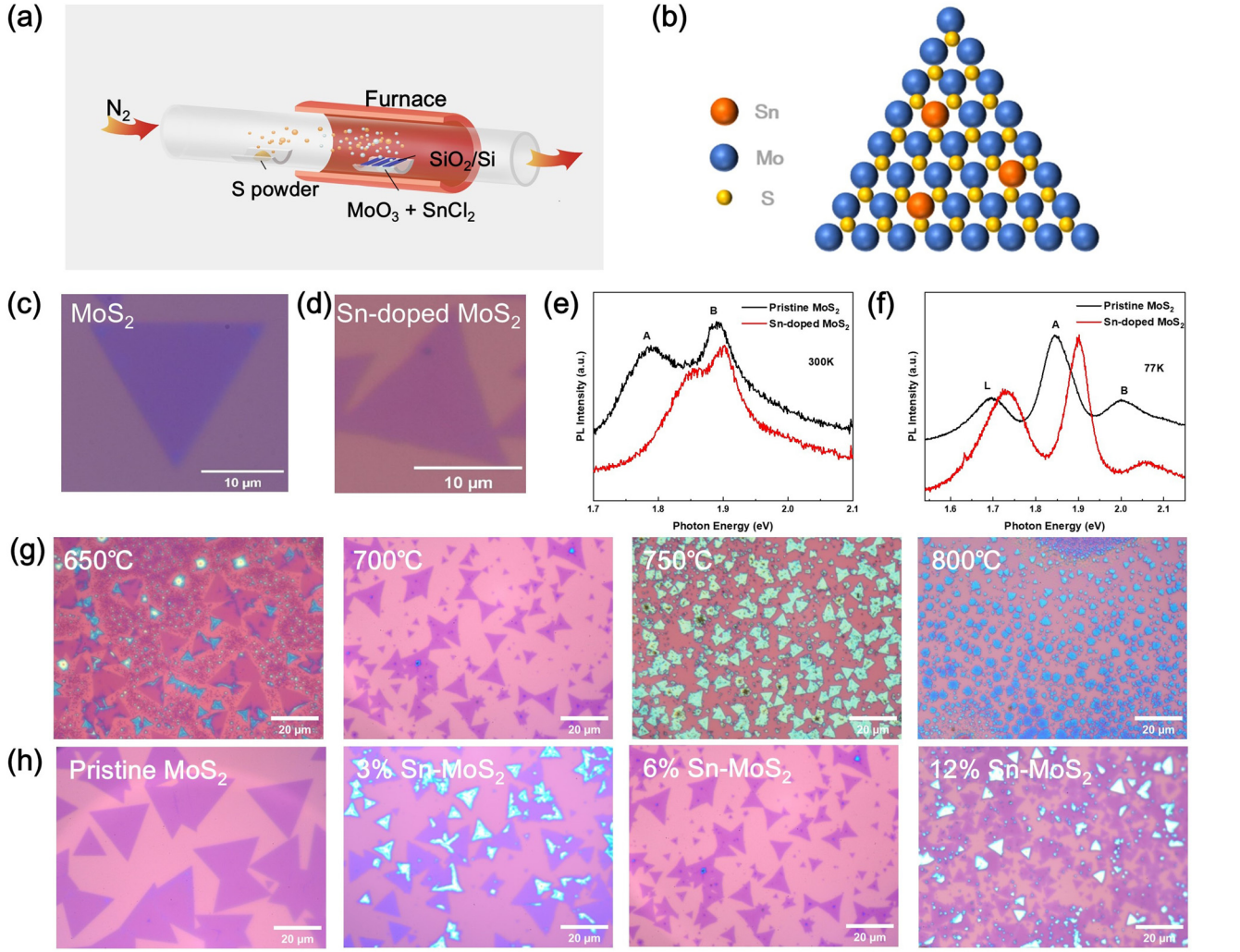

Fig. 1 Synthesis of Sn-doped monolayer MoS_2 single crystals. (a) Illustration of the CVD setup for the synthesis of Sn-doped MoS_2. (b) Schematic of an Sn-doped MoS_2 structure. (c and d) Optical images of pristine MoS_2 and Sn-doped MoS_2, respectively. (e) PL spectra of pristine MoS_2 and Sn-doped MoS_2 at room temperature (532 nm CW laser, 100 μW). (f) PL spectra of pristine MoS_2 and Sn-doped MoS_2 at 77 K (532 nm CW laser, 100 μW). (g) Optical images of 6 wt% $SnCl_2$-doped MoS_2 at the growth temperatures of 650 °C, 700 °C, 750 °C and 800 °C, respectively. (h) Optical images of pristine MoS_2, 3 wt% Sn-doped MoS_2, 6 wt% Sn-doped MoS_2 and 12 wt% Sn-doped MoS_2 at 700 °C.

nent blueshift of the PL emissions from different excitonic states as shown in Fig. 1(e and f). Hence, we conducted further spatial homogeneous measurements to identify the Sn-doped MoS_2, including SEM-EDS, SHG, AFM, Raman, PL and broadband reflectance contrast.

Characterization of Sn-doped MoS_2

The spatial homogeneity of pristine MoS_2 and 3 wt%, 6 wt%, and 12 wt% Sn-doped MoS_2 was identified with scanning electron microscopy (SEM) and PL mapping, respectively. As shown in Fig. 2(a), the pristine MoS_2 crystals have clear boundaries and smooth surfaces, which coincide with the observations of optical images. For 3 wt% Sn-doped MoS_2, the boundary of the crystals changes from a straight line to an irregular convex edge, which indicates that the Sn-doping induces strong strain during the chemical vapor deposition process. When the doping concentration is increased to 6 wt%, the boundaries of MoS_2 crystals become rough, which may be related to the edge growth kinetics.[36,37] However, when the doping concentration reaches 12 wt%, the three corners of the triangular shapes of MoS_2 crystals become rounded, and small nucleation centers in the center of the MoS_2 crystals could be observed. PL mapping images in Fig. 2(b) further demonstrate the high-quality and relatively homogeneous nature of the monolayer single crystals formed. Compared with the pristine MoS_2, the 3 wt% and 6 wt% Sn-doped MoS_2 crystals manifest more excellent homogeneity of PL emissions across the whole sheet of flakes. However, the PL mapping image of 12 wt% Sn-doped MoS_2 shows PL emission concentrated at the edge but weak emission at the center part, suggesting that the high doping concentration leads to the damage of the crystals during the CVD growth. In addition, the PL emission intensity

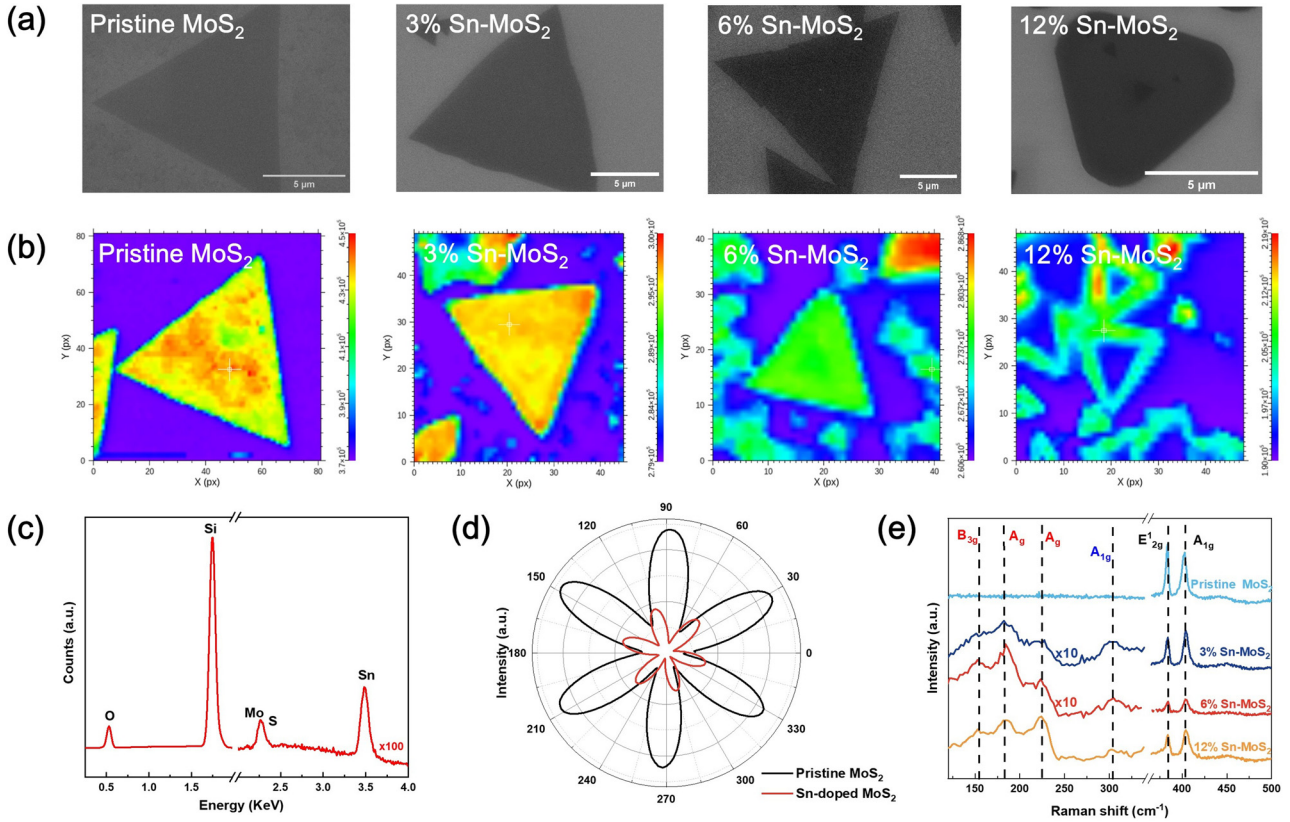

Fig. 2 (a) SEM images corresponding to pristine MoS_2 and 3 wt%, 6 wt%, and 12 wt% Sn-doped MoS_2. (b) PL mapping images corresponding to pristine MoS_2 and 3 wt%, 6 wt%, and 12 wt% Sn-doped MoS_2. (c) EDS spectrum of 6 wt% Sn-doped MoS_2. (d) Second harmonic generation (SHG) intensity of pristine MoS_2 and 6 wt% Sn-doped MoS_2. (e) Raman spectra of MoS_2 with different Sn-doping concentrations.

of the Sn-doped MoS_2 crystals experiences an attenuation trend with the increase of doping concentration.

We performed EDS analysis to confirm the doping of Sn in the Sn-doped MoS_2 crystal. As shown in Fig. 2(c), the Mo and S elements are located at ~2.5 keV, and the peak of ~3.6 keV corresponds to the Sn element, indicating the successful introduction of Sn into the monolayer MoS_2 nanosheet to generate the Sn-doped MoS_2 single crystal, and the doping concentration of the Sn element shows a gradient increase with the increase in the proportion of the precursor (the atomic percentage of Sn rises from 0.29 at% to 0.39 at%), while the total atomic percentages of Mo and S does not fluctuate significantly (Fig. S1†). In order to further probe the lattice symmetry of the Sn-doped MoS_2 crystals, polarization-resolved SHG measurement was performed on the pristine and 6 wt% Sn-doped MoS_2 crystals (Fig. 2(d)). It is shown that both the pristine MoS_2 and Sn-doped MoS_2 have a six-fold polarization symmetry of the SHG signal, which is consistent with the three rotational symmetry of a monolayer MoS_2 single crystal. 3 wt% and 12 wt% Sn-doped MoS_2 are presented in Fig. S2,† also indicating that Sn-doping does not impose the crystal symmetry of MoS_2. It is worth noting that the Sn-doped MoS_2's SHG intensity shrinks compared to the pristine MoS_2, which might be due to the strain induced by Sn-doping.[38] Raman spectroscopy was employed to identify the Raman characteristic modes of pristine MoS_2 and different concentrations of $SnCl_2$-doped MoS_2 single crystals (Fig. 2(e)). The pristine MoS_2 shows two apparent peaks located at 383.8 and 403 cm^{-1}, ascribed to E^1_{2g} and A_{1g} characteristic phonon modes of MoS_2. As for the different Sn-doped MoS_2 crystals, the E^1_{2g} and A_{1g} peaks exhibit characteristic blue-shifts (Fig. S3†). The subtle variations in peak separation (Δ ~0.74 cm^{-1}) likely arise from competing effects of localized lattice distortion induced by dopant atoms, non-uniform charge redistribution between Mo and S atoms, and strain field heterogeneity at different doping levels. At 3 wt% doping, sparse Sn distribution induces localized lattice distortions amplified by size mismatch and synergistic interactions with point defects, leading to significant but spatially confined tensile effects. At 12 wt% doping, accumulated lattice mismatch and strain between aggregated dopants dominate, with potential phase transitions further releasing transient strain. In contrast, the 6% dosage achieves optimal balance: uniform Sn distribution minimizes local strain while compensating intrinsic defects (*e.g.*, sulfur vacancies), thereby suppressing detectable global peak shifts. In particular, four relatively weak peaks, located at 154.1, 182.4, 223.9 and 302.3 cm^{-1}, emerge in all of the Sn-doped MoS_2 crystals, corresponding to the B_{3g} and A_g peaks of SnS and the A_{1g} peak

of SnS_2, which indicates that the $SnCl_2$-dopant has decomposed and the Sn element has occupied some positions of Mo in the lattice point to form SnS and SnS_2 in Sn-MoS_2. It is worth noting that the peak intensities increase with the increasing concentration of $SnCl_2$. Compared with pure SnS single crystals,[39] the B_{3g} and A_g peaks of SnS have distinct red shifts of 4.5 and 5.7 cm^{-1}, respectively; instead, the higher wavenumber peak of A_g has a blueshift of 7.2 cm^{-1}, which manifests that strong strain exists in the Sn-doped MoS_2 crystal. This originates from the relatively huge difference in lattice constants between SnS (SnS_2) and MoS_2. In addition, the wavenumber differences for E^1_{2g} and A_{1g} of the pristine MoS_2 and 3 wt%, 6 wt%, and 12 wt% Sn-doped MoS_2 are all ~19 cm^{-1}. AFM characterization (Fig. S4†) shows some variation from the theoretical monolayer thickness (~0.65 nm), but they all remain below the bilayer threshold (~1.2 nm). The increased thickness in doped samples likely stems from three factors: (1) local lattice expansion due to Sn incorporation, (2) surface adsorbates from the doping process, and (3) slight out-of-plane distortions induced by strain. Crucially, this interpretation is strongly supported by Raman (Fig. S3†) and PL spectra (Fig. 3), which collectively verify the monolayer nature across all samples, suggesting that the nature of monolayer MoS_2 crystals retain a high quality and less damage after Sn-doping.

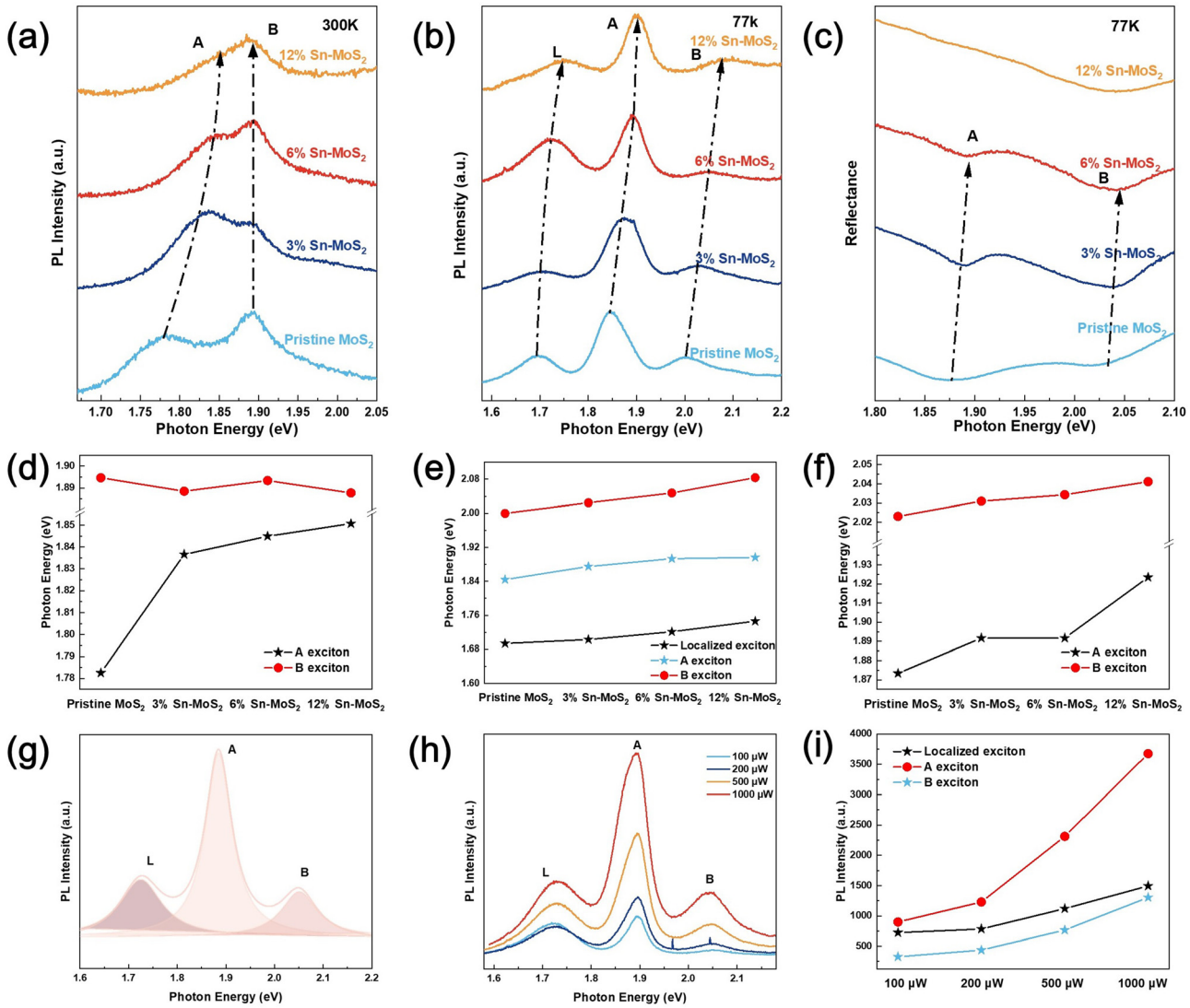

Fig. 3 Optical properties for different concentrations of $SnCl_2$-doping MoS_2. (a) PL spectra of pristine MoS_2 and 3 wt%, 6 wt%, and 12 wt% Sn-doped MoS_2 at room temperature (532 nm CW laser, 100 μW, 30 s). (b) PL spectra of pristine MoS_2 and 3 wt%, 6 wt%, and 12 wt% Sn-doped MoS_2 at 77 K (532 nm CW laser, 200 μW, 30 s). (c) Reflectance spectra of pristine MoS_2 and 3 wt%, 6 wt%, and 12 wt% Sn-doped MoS_2 at 77 K. (d) Photon energies of A excitons and B excitons as a function of doping concentration at room temperature extracted from (a). (e) Photon energies of localized defect excitons, A excitons and B excitons as a function of doping concentration at 77 K extracted from (b). (f) Absorption photon energies of A excitons and B excitons as a function of doping concentration at 77 K extracted from (c). (g) Lorentzian fitting for different excitonic states of 6 wt% Sn-doped MoS_2 at 77 K. (h) PL spectra of 6 wt% Sn-doped MoS_2 with incident power values of 100, 200, 500 and 1000 μW at 77 K. (i) Integrated PL intensities of localized defect excitons, A excitons and B excitons of 6 wt% Sn-doped MoS_2 as a function of incident power at 77 K.

Since Sn-doping dramatically imposes the growth behavior and the homogeneity of MoS_2, it is important to further reveal the effect of Sn-doping on the electronic states, thus renormalizing the band structure of MoS_2. In Fig. 3(a and b), the PL spectra of Sn-doped MoS_2 at room temperature and 77 K show a blueshift compared to that of pristine MoS_2, in which the photon energies of A and B and localized defect exciton states continuously increase with the increasing Sn-doping concentration. The photon energy of A excitons of MoS_2 is blueshifted from 1.783 eV to 1.850 eV with increasing doping concentration with an energy difference of ~70 meV, whereas the effect on B excitons is not obvious at room temperature. The low-temperature environment significantly reduces the lattice vibration and thermal dissociation effects, allowing the radiative complexation process of localized excitons to dominate, thus their corresponding luminescence peaks are significantly enhanced in intensity, the spectral line widths are narrowed, and the positions of the characteristic peaks are more pronounced. Therefore, the peak-resolved spectra at 77 K provide better accuracy in extracting the photon energy blue shifts of A exciton, B exciton and localized defect exciton states at 50 meV, 80 meV and 50 meV, respectively. In addition, we also obtained the broadband reflectance contrast for pristine MoS_2, 3 wt%, 6 wt%, and 12 wt% Sn-doped MoS_2 as shown in Fig. 3(c). It is obvious that the absorptions for A excitons and B excitons also experience a blueshift in photon energy, which further confirms that the blueshift of all exciton energies comes from the renormalization of the band structure with Sn-doping. As shown in Fig. 3(g–i), we used Lorentzian peak fitting of the PL spectra of 6 wt% Sn-doped MoS_2 at 77 K to extract the integrated PL emission intensities for different excitonic states as a function of excitation power. It reveals that the PL intensities of all exciton states show a superlinear enhancement as a function of the incident power. The excitation power dependent PL spectra for pristine MoS_2 and 3 wt% and 12 wt% Sn-doped MoS_2 both at room temperature and 77 K can be found in Fig. S6 and S7 in the ESI,† which display similar superlinear enhancement behavior.

The variation of PL intensity with the doping concentration of $SnCl_2$ at room temperature and 77 K is shown in Fig. S5,† where not only the photon energy of each exciton state retains the blueshift response but also the PL intensity monotonically decreases with the increasing doping concentration, consistent with PL spectra in Fig. 3 and the PL mapping images shown in Fig. 2(b). These phenomena further prove that the Sn-doping effect remarkably imposes the electronic structure of MoS_2 with the enlargement of the bandgap and the possible transformation from a direct bandgap to an indirect bandgap, which will be further discussed in the following section.

Discussion

Based on the above growth characterization and the optical properties of pristine and Sn-doped MoS_2, we can derive the effect of $SnCl_2$-doping on monolayer MoS_2 single crystals as follows[40] (Fig. 4(a)): first, the $SnCl_2$ dopant decomposes into a free Sn atom and chlorine gas upon heating to a temperature of 247 °C,[41] which deposits on the 300 nm SiO_2/Si substrate as the nucleating point for the imminent growth of MoS_2. As the temperature increases to 500 °C (S powder at a temperature of 120 °C) and the sulfur vapor starts to be conveyed to the deposition site[42,43] to react with the vapor of the precursor MoO_3, forming Sn-doped MoS_2 crystals at the nucleating points of Sn atoms,[44,45] demonstrated by the coexistence of Raman characterization modes for SnS, SnS_2 and MoS_2 as shown in Fig. 2(e). Meanwhile, the bond length of Sn–S (2.59 Å) is longer than that of the Mo–S bond (2.41 Å),[46] resulting in the different lattice constants of SnS, SnS_2 and MoS_2, which have ~15.7% lattice mismatch between SnS_2 and MoS_2 and ~16.8% between SnS and MoS_2, respectively.[47,48] As shown in Fig. 4(b), the lattice mismatch between SnS/SnS_2 and MoS_2 gives rise to a

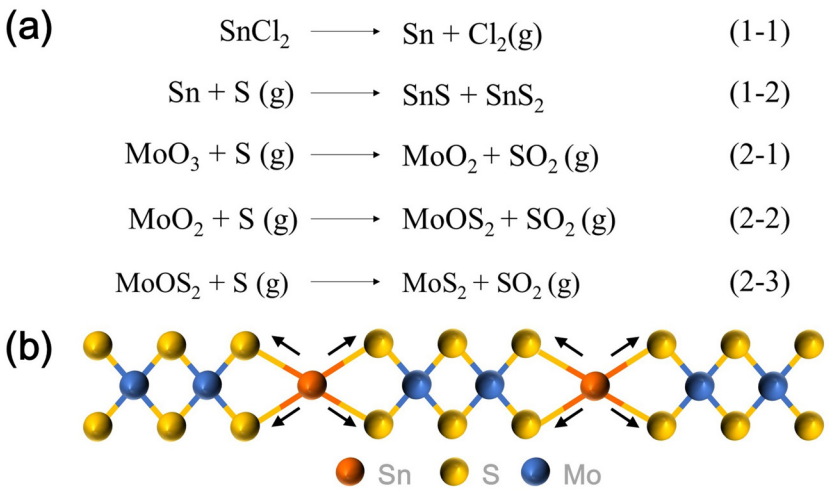

Fig. 4 (a) Reaction formulae involved in the CVD synthesis of molybdenum disulfide. (b) Schematic representation of the mechanism of Sn-doped monolayer MoS_2.

lateral strain to induce a local out-of-plane curvature, which will dramatically impose the renormalization of the band structure,[49] consistent with previous theoretical and experimental results.[46] The blue shift and intensity weakening observed in the PL spectra after Sn doping of MoS_2 might have originated from the combined effect of the direct-to-indirect band structure transition and tensile strain.

First, it can be seen from Fig. S3† that the introduction of Sn doping leads to blue shifts of E^1_{2g} and A_{1g} in MoS_2, and with 3 wt% Sn-MoS_2, the sparsely distributed dopant atoms cause local lattice distortions and defect effects, leading to significant tensile strains. For 12 wt% Sn-MoS_2, a large number of dopant atoms exacerbate the lattice mismatches and strain accumulations, and may even induce a phase transition or structural remodeling, further increasing the strains. This tensile strain changes the Mo–S bond length and bond angle, thus regulating its energy band structure (Fig. 4(b)). This tensile strain not only increases the bandgap but also may lead to the transformation of MoS_2 from a direct bandgap semiconductor to an indirect bandgap semiconductor (Fig. S8†). The direct-to-indirect band structure transition makes the electron–hole recombination require phonon participation, which significantly reduces the radiative compounding efficiency and leads to a weakening of the PL intensity. In addition, the defects introduced by Sn doping (*e.g.*, sulfur vacancies or Sn atom substitution sites) act as nonradiative composite centers, increasing the nonradiative composite probability of electron–hole pairs and further decreasing the PL intensity. In summary, after Sn doping of MoS_2, the effects of tensile strain and defect states lead to a change in the energy band structure, which transforms MoS_2 from a direct bandgap to an indirect bandgap semiconductor, and thus induces a blue shift in the PL spectra and a reduction in the intensity.

Conclusions

In summary, we have developed a new method using $SnCl_2$ as an efficient dopant to grow a Sn-doped MoS_2 monolayer. The Sn-doped MoS_2 monolayer dramatically imposes the growth behavior and the electronic state of MoS_2 due to the lattice mismatch between SnS (SnS_2) and MoS_2, resulting in the renormalization of the band structure with the enlargement of the bandgap and the possible shift from a direct bandgap to an indirect in the monolayer MoS_2. The developed Sn-doping method could serve as an effective approach to tailor the band structure and explore a plethora of fascinating optical and electronic properties in 2D TMDCs, paving the way for the next generation of optoelectronic devices.

Methods

CVD growth

Sn-doped MoS_2 was synthesized by an atmospheric pressure CVD method in a single temperature tube furnace as depicted in Fig. 1(a). A mixture of 14 mg MoO_3 with $SnCl_2$ powder (0.5 mg, 1 mg, 2 mg) was placed in a quartz boat. The SiO_2/Si substrate was inverted onto a quartz boat and placed at the center of the tube furnace. Another quartz boat containing 120 mg of sulfur powder was placed around 16 cm upstream of the molybdenum oxide precursor. The CVD process was carried out at ambient pressure and high-purity N_2 was used as the carrier gas. The furnace temperature was raised to 700 °C at a rate of 14 °C min^{-1} and held for 5 min with the carrier gas flow rate maintained at 10 sccm. Then, the furnace was rapidly cooled down to room temperature at a carrier gas flow rate of 500 sccm and Sn-doped MoS_2 was obtained on the SiO_2/Si substrate (Fig. S9†).

Characterization of Sn-doped MoS_2 monolayers

SEM was performed using an Apreo 2S model from Thermo Fisher with an accelerating voltage of 15.00 kV. Raman and PL spectra of Sn-doped MoS_2 were collected with an Andor spectrometer using a 532 nm CW laser and the Raman signal was calibrated from the peak of silicon (520 cm^{-1}). PL mapping images were obtained using a 532 nm CW laser with a 10 mW power for 0.1 s. The polarization-resolved SHG was evaluated using a home-built setup with the excitation wavelength of an 810 nm femtosecond pulse laser (Chameleon Ultra II, with a pulse width of 140 fs and a repetition rate of 80 MHz). The pulse laser was focused by a 40× objective, and the focused laser spot was about 2 μm.

Data availability

The data that support the findings of this study are available from the corresponding author upon reasonable request.

Conflicts of interest

The authors declare no competing financial interest.

Acknowledgements

This work is supported by the National Natural Science Foundation of China (Grant No. 52272158) and the Natural Science Foundation of Shanghai (Grant No. 23ZR1431200). We also acknowledge the support from the Fundamental Research Funds for the Central Universities (No. YG2024ZD28 and No. YG2023QNA26) and the Shenzhen Medical Research Fund (No. A2403056).

References

1 N. Li, Q. Wang, C. Shen, Z. Wei, H. Yu, J. Zhao, X. Lu, G. Wang, C. He, L. Xie, J. Zhu, L. Du, R. Yang, D. Shi and G. Zhang, *Nat. Electron.*, 2020, **3**, 711–717.

2 X. Liu and M. C. Hersam, *Nat. Rev. Mater.*, 2019, **4**, 669–684.
3 N. Rohaizad, C. C. Mayorga-Martinez, M. Fojtů, N. M. Latiff and M. Pumera, *Chem. Soc. Rev.*, 2021, **50**, 619–657.
4 S. B. Desai, S. R. Madhvapathy, A. B. Sachid, J. P. Llinas, Q. Wang, G. H. Ahn, G. Pitner, M. J. Kim, J. Bokor, C. Hu, H.-S. P. Wong and A. Javey, *Science*, 2016, **354**, 99–102.
5 S. Wachter, D. K. Polyushkin, O. Bethge and T. Mueller, *Nat. Commun.*, 2017, **8**, 14948.
6 H. Zhang, *Chem. Rev.*, 2018, **118**, 6089–6090.
7 B. Radisavljevic, A. Radenovic, J. Brivio, V. Giacometti and A. Kis, *Nat. Nanotechnol.*, 2011, **6**, 147–150.
8 V. Nicolosi, M. Chhowalla, M. G. Kanatzidis, M. S. Strano and J. N. Coleman, *Science*, 2013, **340**, 1226419.
9 C. Muratore and A. A. Voevodin, *Thin Solid Films*, 2009, **517**, 5605–5610.
10 C. Muratore, V. Varshney, J. J. Gengler, J. Hu, J. E. Bultman, A. K. Roy, B. L. Farmer and A. A. Voevodin, *Phys. Chem. Chem. Phys.*, 2014, **16**, 1008–1014.
11 B. Wang, Y. Xia, J. Zhang, H.-P. Komsa, M. Xie, Y. Peng and C. Jin, *Nano Res.*, 2020, **13**, 1889–1896.
12 L. Li, Q. Wang, F. Wu, Q. Xu, J. Tian, Z. Huang, Q. Wang, X. Zhao, Q. Zhang, Q. Fan, X. Li, Y. Peng, Y. Zhang, K. Ji, A. Zhi, H. Sun, M. Zhu, J. Zhu, N. Lu, Y. Lu, S. Wang, X. Bai, Y. Xu, W. Yang, N. Li, D. Shi, L. Xian, K. Liu, L. Du and G. Zhang, *Nat. Commun.*, 2024, **15**, 1825.
13 M. Xu, H. Ji, L. Zheng, W. Li, J. Wang, H. Wang, L. Luo, Q. Lu, X. Gan, Z. Liu, X. Wang and W. Huang, *Nat. Commun.*, 2024, **15**, 562.
14 J. Wang, X. Xu, T. Cheng, L. Gu, R. Qiao, Z. Liang, D. Ding, H. Hong, P. Zheng, Z. Zhang, Z. Zhang, S. Zhang, G. Cui, C. Chang, C. Huang, J. Qi, J. Liang, C. Liu, Y. Zuo, G. Xue, X. Fang, J. Tian, M. Wu, Y. Guo, Z. Yao, Q. Jiao, L. Liu, P. Gao, Q. Li, R. Yang, G. Zhang, Z. Tang, D. Yu, E. Wang, J. Lu, Y. Zhao, S. Wu, F. Ding and K. Liu, *Nat. Nanotechnol.*, 2022, **17**, 33–38.
15 J. Yu, J. Li, W. Zhang and H. Chang, *Chem. Sci.*, 2015, **6**, 6705–6716.
16 K. S. Novoselov, A. Mishchenko, A. Carvalho and A. H. Castro Neto, *Science*, 2016, **353**, aac9439.
17 J. S. Lee, C.-S. Park, T. Y. Kim, Y. S. Kim and E. K. Kim, *Nanomaterials*, 2019, **9**, 1278.
18 V. P. Pham and G. Y. Yeom, *Adv. Mater.*, 2016, **28**, 9024–9059.
19 Y. Lin, R. Torsi, D. B. Geohegan, J. A. Robinson and K. Xiao, *Adv. Sci.*, 2021, **8**, 2004249.
20 H. Xu, H. Zhang, Y. Liu, S. Zhang, Y. Sun, Z. Guo, Y. Sheng, X. Wang, C. Luo, X. Wu, J. Wang, W. Hu, Z. Xu, Q. Sun, P. Zhou, J. Shi, Z. Sun, D. W. Zhang and W. Bao, *Adv. Funct. Mater.*, 2019, **29**, 1805614.
21 J. Jiang, L. Xu, L. Du, L. Li, G. Zhang, C. Qiu and L.-M. Peng, *Nat. Electron.*, 2024, **7**, 545–556.
22 Y. Jin, Z. Zeng, Z. Xu, Y.-C. Lin, K. Bi, G. Shao, T. S. Hu, S. Wang, S. Li, K. Suenaga, H. Duan, Y. Feng and S. Liu, *Chem. Mater.*, 2019, **31**, 3534–3541.
23 X. Li, J. Yang, H. Sun, L. Huang, H. Li and J. Shi, *Adv. Mater.*, 2023, 2305115.
24 Y. Chen, Y. Jiang, C. Yi, H. Liu, S. Chen, X. Sun, C. Ma, D. Li, C. He, Z. Luo, F. Jiang, W. Zheng, B. Zheng, B. Xu, Z. Xu and A. Pan, *Sci. China Mater.*, 2021, **64**, 1449–1456.
25 W. Wang, H. Shu, J. Wang, Y. Cheng, P. Liang and X. Chen, *ACS Appl. Mater. Interfaces*, 2020, **12**, 9563–9571.
26 P. Man, S. Jiang, K. H. Leung, K. H. Lai, Z. Guang, H. Chen, L. Huang, T. Chen, S. Gao, Y. Peng, C. Lee, Q. Deng, J. Zhao and T. H. Ly, *Adv. Mater.*, 2024, **36**, 2304808.
27 P. Wang, J. Qu, Y. Wei, H. Shi, J. Wang, X. Sun, W. Li, W. Liu and B. Gao, *ACS Appl. Mater. Interfaces*, 2021, **13**, 58144–58151.
28 L. Fang, L. Su, H. Guan, Z. Liu, Y. Yu, D. Cao, X. Chen and H. Shu, *ACS Appl. Nano Mater.*, 2024, **7**, 5063–5073.
29 S. Li, X. Chen, F. Liu, Y. Chen, B. Liu, W. Deng, B. An, F. Chu, G. Zhang, S. Li, X. Li and Y. Zhang, *ACS Appl. Mater. Interfaces*, 2019, **11**, 11636–11644.
30 M. Okada, N. Nagamura, T. Matsumura, Y. Ando, A. K. A. Lu, N. Okada, W.-H. Chang, T. Nakanishi, T. Shimizu, T. Kubo, T. Irisawa and T. Yamada, *APL Mater.*, 2021, **9**, 121115.
31 D. Xu, P. Jian, W. Liu, S. Tan, Y. Yang, M. Peng, J. Dai, C. Chen and F. Wu, *ACS Appl. Mater. Interfaces*, 2024, **16**, 23771–23779.
32 R.-J. Chang, Y. Sheng, G. H. Ryu, N. Mkhize, T. Chen, Y. Lu, J. Chen, J. K. Lee, H. Bhaskaran and J. H. Warner, *ACS Appl. Mater. Interfaces*, 2019, **11**, 24279–24288.
33 J. N. Olding, A. Henning, J. T. Dong, Q. Zhou, M. J. Moody, P. J. M. Smeets, P. Darancet, E. A. Weiss and L. J. Lauhon, *ACS Appl. Mater. Interfaces*, 2019, **11**, 40543–40550.
34 Q. Fu, Q. Wu, X. Zhang, Z. Cai, K. K. Ostrikov, X. Gu, H. Nan and S. Xiao, *ACS Appl. Nano Mater.*, 2022, **5**, 14978–14986.
35 X. Xu, T. Guo, H. Kim, M. K. Hota, R. S. Alsaadi, M. Lanza, X. Zhang and H. N. Alshareef, *Adv. Mater.*, 2022, **34**, 2108258.
36 C. Cong, J. Shang, X. Wu, B. Cao, N. Peimyoo, C. Qiu, L. Sun and T. Yu, *Adv. Opt. Mater.*, 2014, **2**, 131–136.
37 S. Wang, Y. Rong, Y. Fan, M. Pacios, H. Bhaskaran, K. He and J. H. Warner, *Chem. Mater.*, 2014, **26**, 6371–6379.
38 L. Mennel, M. Paur and T. Mueller, *APL Photonics*, 2019, **4**, 034404.
39 Z. Tian, C. Guo, M. Zhao, R. Li and J. Xue, *ACS Nano*, 2017, **11**, 2219–2226.
40 J. V. Pondick, J. M. Woods, J. Xing, Y. Zhou and J. J. Cha, *ACS Appl. Nano Mater.*, 2018, **1**, 5655–5661.
41 L. Huang, Z. Hu, H. Jin, J. Wu, K. Liu, Z. Xu, J. Wan, H. Zhou, J. Duan, B. Hu and J. Zhou, *Adv. Funct. Mater.*, 2020, **30**, 1908486.
42 A. M. Van Der Zande, P. Y. Huang, D. A. Chenet, T. C. Berkelbach, Y. You, G.-H. Lee, T. F. Heinz, D. R. Reichman, D. A. Muller and J. C. Hone, *Nat. Mater.*, 2013, **12**, 554–561.
43 Q. Ji, C. Su, N. Mao, X. Tian, J.-C. Idrobo, J. Miao, W. A. Tisdale, A. Zettl, J. Li and J. Kong, *Sci. Adv.*, 2021, **7**, eabj3274.
44 C.-M. Hyun, J.-H. Choi, S. W. Lee, J. H. Park, K.-T. Lee and J.-H. Ahn, *J. Alloys Compd.*, 2018, **765**, 380–384.

45 H. F. Liu, S. L. Wong and D. Z. Chi, *Chem. Vap. Deposition*, 2015, **21**, 241–259.
46 Q. Zhang, H. Ying, X. Li, R. Xiang, Y. Zheng, H. Wang, J. Su, M. Xu, X. Zheng, S. Maruyama and X. Zhang, *ACS Appl. Mater. Interfaces*, 2021, **13**, 31861–31869.
47 M. Farmanbar and G. Brocks, *Phys. Rev. B*, 2016, **93**, 085304.
48 J. Liu and J. Zhang, *Chem. Rev.*, 2020, **120**, 2123–2170.
49 L. Yang, X. Cui, J. Zhang, K. Wang, M. Shen, S. Zeng, S. A. Dayeh, L. Feng and B. Xiang, *Sci. Rep.*, 2014, **4**, 5649.